

SIMULATIONS OF ZERO PRESSURE-GRADIENT TURBULENT BOUNDARY LAYERS OVER RIBLETS

V. Kumar¹, A. Rouhi², O. Lehmkuhl¹, W. Wu³, M. Kozul⁴ and A. J. Smits⁵

¹ CASE, Barcelona Supercomputing Center (BSC), Barcelona, Spain

² Department of Engineering, Nottingham Trent University, Nottingham, UK

³ Department of Mechanical Engineering, University of Mississippi, Oxford, USA

⁴ Department of Mechanical Engineering, University of Melbourne, Melbourne, Australia

⁵ Department of Mechanical and Aerospace Engineering, Princeton University, Princeton, USA
vishal.kumar@bsc.es

Abstract

We computationally study the response of zero-pressure-gradient (ZPG) turbulent boundary layers (TBLs) to streamwise step changes from a smooth wall to riblets (S-R), and vice versa (R-S). We consider triangular riblets with tip angle 90° (T9), that increase drag, with viscous-scaled spacing 50. A novel grid-generation approach is developed for unstructured spectral-element codes, consistent with the size of turbulent scales across the TBL. We generate a ZPG TBL upstream of the step change (with thickness δ_0) with momentum thickness Reynolds number $Re_{\theta_0} \simeq 680$. The TBL departure from equilibrium due to the step change, and its subsequent relaxation, recall previous studies on step changes in surface roughness. Downstream of the R-S step change, the internal equilibrium layer thickness δ_{IEL} reaches $0.4\delta_0$ within $12\delta_0$. However, downstream of the S-R step change δ_{IEL} reaches $0.4\delta_0$ within $4\delta_0$. In all cases, δ_{IEL} does not reach the boundary layer thickness, even up to a distance of $45\delta_0$ downstream of the step change, owing to persistent history effects within the frozen wake region.

1 Introduction

Riblets are streamwise-aligned grooves that modify the structure of the near-wall turbulence. Depending on their dimensions in viscous units, they can reduce or increase turbulent skin-friction drag (Endrikat et al., 2021). Over the past four decades, numerous studies have investigated the physical mechanisms behind riblet-induced drag modification. Most computational studies have focused on canonical turbulent channel flows (Modesti et al. 2021; Rouhi et al. 2022), whereas experimental investigations have predominantly considered zero-pressure-gradient (ZPG) turbulent boundary layers (TBLs) (Choi 1989).

A limited number of computational studies have examined riblet effects in TBLs (e.g., Bannier et al. 2015; Boomsma and Sotiropoulos 2015). These works typically generate a turbulent inflow using techniques developed for smooth walls, such as recycling-rescaling or synthetic eddy methods. Conse-

quently, the computational setup consists of a smooth wall, followed by a step change to riblets. Such a surface transition disturbs the equilibrium state of the TBL, which requires some downstream distance to recover.

Abrupt changes in wall texture, for example smooth-to-roughness and vice-versa, trigger a localized yet persistent perturbation to the flow, leading to its departure from equilibrium (Antonia & Luxton 1971). Flow recovery to its new equilibrium state downstream of the step change depends on various parameters, such as geometrical characteristics of surfaces, and Reynolds number (Rouhi et al. 2019, Li et al. 2019). The flow recovery to equilibrium is a bottom-up process from the surface underneath, and is quantified via the internal boundary layer (IBL) and internal equilibrium layer (IEL). The IBL is the region of the flow that ‘feels’ the presence of the new wall condition, while maintaining upstream history outside of it (Garratt 1990). The IEL is the part of the IBL where the flow has reached complete equilibrium with the surface underneath (Savelyev & Taylor 2005).

In the present study we pursue two objectives: 1) to develop an inflow generation approach to achieve a ZPG TBL over riblets, yet avoiding the smooth-to-riblets surface change, as employed in the past computational investigations, and 2) study the flow recovery to equilibrium downstream of the step changes from smooth-to-riblets, and vice versa.

2 Methodology

Governing equations and numerical discretization

We solve the incompressible conservation of mass and momentum flow equations with constant density ρ and kinematic viscosity ν :

$$\nabla \cdot \mathbf{u} = 0. \quad (1a)$$

$$\frac{\partial \mathbf{u}}{\partial t} + \nabla \cdot (\mathbf{u}\mathbf{u}) = -\frac{1}{\rho} \nabla p + \nu \nabla^2 \mathbf{u}. \quad (1b)$$

Where $\mathbf{u} = (u, v, w)$ is the velocity vector, and x, y, z are the streamwise, wall-normal and spanwise directions, respectively. Equations (1a,b) are solved using

Case	Δ_x^+	Δ_ξ^+	Δ_z^+	Δ_y^+
T950_coarse	20.0	1.0	0.7 – 4.0	0.7 – 8.1
T950_fine	10.0	1.0	0.7 – 4.0	0.7 – 8.1
T615_coarse	10.0	0.6	0.3 – 12.0	0.25 – 7.87
T615_fine	7.0	0.4	0.2 – 8.2	0.17 – 5.13

Table 1: Simulation cases for turbulent half-channel flow over T950 and T615 riblets; Δ_ξ^+ is the viscous-scaled azimuthal grid size over the riblets. For all cases, the domain size is $L_x \times L_z \simeq 6h \times 3h$, where h is the half-channel height.

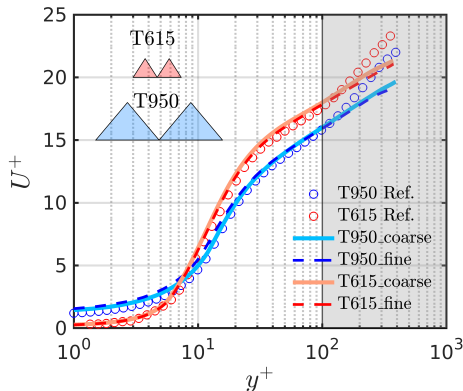


Figure 1: Mean velocity profiles for the cases from Table 1 compared with the reference data of Endrikat et al. (2021). The shaded region ($y^+ > 100$) is discarded from comparison, as the profiles of Endrikat et al. (2021) are from a reduced-domain channel flow simulation.

a well-validated computational solver (SOD2D) developed at Barcelona Supercomputing Center. Spatial discretization is based on a spectral formulation of the Continuous Galerkin Finite Elements model, coupled with an entropy viscosity stabilization (Guermont et al. 2011). We utilize third-order hexahedral element based mesh for all our calculations. Time advancement is 2^{nd} order Adams-Bashforth for the convection terms, and 2^{nd} order Crank-Nicolson for the diffusion terms. High-order operator splitting approach is used to solve the velocity–pressure coupling (Karniadakis et al. 1991). Numerical details for SOD2D are reported in Gasparino et al. (2024).

Code verification

We assess the accuracy of SOD2D and its resolution requirements for riblets by replicating the turbulent channel flow cases of Endrikat et al. (2021) at friction Reynolds number $Re_\tau = 400$ over two triangular riblet geometries; one with tip angle $\alpha = 90^\circ$ and viscous-scaled spacing $s^+ = 50$ (termed T950), and another one with $\alpha = 60^\circ$ and $s^+ = 15$ (termed T615). These geometries were selected based on their known drag characteristics: T950 increases drag, while T615 reduces drag, compared to the smooth channel. Table 1 lists the resolutions used for the cal-

culational cases. For T950, the *coarse* and *fine* cases differ in the streamwise resolution, *fine* being the typical DNS resolution prescribed in literature. For T615, *coarse* is the typical DNS resolution, while *fine* has about 1.5 times finer grid size in all directions. We obtain very good agreement in the mean velocity profiles with the reference DNS data of Endrikat et al. (2021), even with the coarse grid calculations (figure 1). Our study highlights that even with $\Delta_x^+ = 20$ we obtain as accurate results as those with $\Delta_x^+ = 10$. For T615 cases, we employed a multi-block grid generation approach to save the computational cost (figure 3). We discuss this approach next.

Boundary layer setup

Figure 2(a) presents our setup for ZPG TBL. We set the domain width and height (L_z, L_y) three times of the maximum boundary layer thickness near the outlet, where the momentum thickness Reynolds number reaches $Re_\theta \simeq 1000$ (friction Reynolds number $Re_\tau \simeq 400$). These dimensions are larger than the ZPG TBL setup by Schlatter et al. (2009).

A laminar boundary layer with displacement thickness Reynolds number $Re_{\delta_{in}^*} = 775$ is applied at the inlet. For the setups with the smooth wall at the inlet, we apply a laminar Blasius profile. However, for the cases with riblets at the inlet, we generate the inflow from a precursor calculation of a laminar temporal boundary layer. Slightly downstream of the inlet, we trip the boundary layer via volumetric forcing added to (1b). This forcing mimics the drag force by a trip wire with length and height l_x, l_y , respectively. The equations read,

$$f_x = -\frac{1}{2}\rho C_D u|u|/l_x, \quad f_y = 0, \quad f_z = 0. \quad (2)$$

Here C_D is a constant factor. The forcing is applied for $x_{trip} \leq x \leq x_{trip} + l_x, 0 \leq y \leq l_y$. From a series of calculations, we arrived at the optimal tripping parameters $C_D = 3.0, l_x = l_y = 1.5\delta_{in}^*$ and $x_{trip} = 12\delta_{in}^*$. We apply no-slip condition at the bottom boundary, zero-vorticity condition at the top boundary, and periodic boundary condition in the spanwise direction. At the outlet, we apply a buffer region where the flow retransitions to laminar, following a similar approach as the one by Munters et al. (2016).

Calculation cases

We conduct large-eddy simulations of ZPG TBLs over different surface textures (table 2) with Vreman (2004) subgrid-scale model. A case with an entirely smooth wall (case SM), and a case with an entirely triangular riblets with tip angle $\alpha = 90^\circ$ (case T9). These cases are considered as benchmarks against which we will quantify the flow recovery to equilibrium for the cases with a step change in surface condition. We conduct a case with a riblet-to-smooth step change (T9.SM) from T9 riblets to a smooth wall; right upstream of the step change, the T9 riblets have

$s^+ \simeq 52$, comparable with our validation cases in channel flow (T950 from table 1). As a result, the mean velocity profile of the T9_SM case upstream of the step change agrees well with the T950 profile from channel flow (figure 2b). Our last case (SM_T9) is a step change from a smooth wall to T9 riblets. For the cases with the step change, we place the origin ($x = 0$) at the step change, where $Re_\theta \simeq 670$ ($Re_\tau \simeq 283$), and δ_0 (TBL thickness) is our reference length for scaling. The patch length upstream of the step change is $40\delta_0$, and the one downstream is $80\delta_0$.

Computational grid

For computational efficiency, we generate an optimal locally-varying grid (figure 3), following the resolution prescription of Chen & He (2023). The wall-normal and spanwise grid sizes (Δ_y^+, Δ_z^+) expand gradually from the near-wall region towards the top boundary, consistent with the turbulent scales across the TBL. Near the riblet ($y^+ \leq 1.5k^+$, $k^+ \equiv$ riblet height), we generate a fine grid with $\Delta_\xi^+ = 1$, $\Delta z^+ \leq 1$; plus units is based on the x -location where $\delta^+ = 400$, near the outlet (denoted as δ_{400}^+). We apply $\Delta z^+ \leq 3.0$ up to the beginning of the logarithmic region ($y^+ \simeq 3\sqrt{\delta_{400}^+}$) to well resolve the near-wall cycle of turbulence in the buffer region. Then we increase Δz^+ to 11.0 near the boundary layer edge ($y^+ \simeq \delta_{400}^+$), and further increase that to 25.0 by the top boundary. The wall-normal grid size also grows consistent with Δ_z^+ ($\Delta_y^+ \simeq \Delta_z^+$). With this optimal grid, we highly resolve the flow near the riblets, yet we

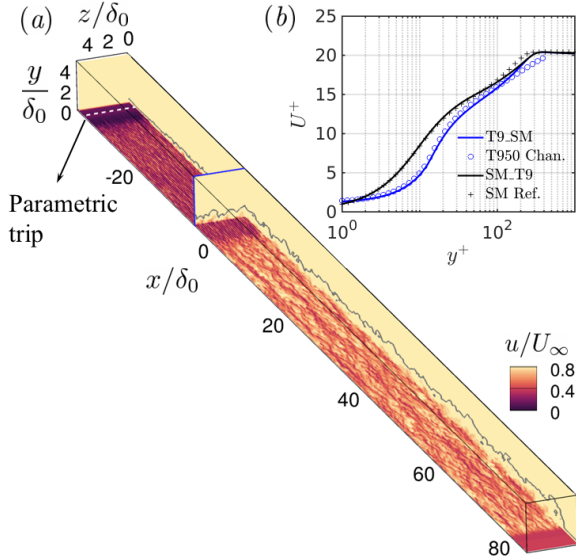


Figure 2: (a) Flow setup and visualization for the case T9_SM. (b) Mean velocity profiles upstream of the step change ($x = -4\delta_0$) for the T9_SM and SM_T9 cases (lines); the profiles are compared with ones from the smooth-wall ZPG TBL of Schlatter et al. (2009), and T950.fine case from Table 1.

Case	L_{SM}	L_{T9}
SM (entirely smooth)	$120\delta_0$	—
T9 (entirely T9)	—	$120\delta_0$
T9_SM (T9 to smooth)	$80\delta_0$	$40\delta_0$
SM_T9 (smooth to T9)	$40\delta_0$	$80\delta_0$

Table 2: Simulation cases for the ZPG TBL over entirely smooth or entirely riblet surfaces, as well as step changes from smooth to riblets, and vice versa; L_{SM} and L_{T9} indicate the length of the smooth and riblet patches, respectively.

do not waste unnecessary grid count above the boundary layer in the inviscid region. We apply a uniform grid in the streamwise direction with $\Delta_x^+ = 20$.

3 Results

We study the variations of Re_θ and C_f for T9_SM (figure 4) and SM_T9 (figure 5). In figure 4, we add case SM, to assess the flow recovery downstream of the T9-to-smooth step change. Similarly, in figure 5 we add case T9 to assess the flow recovery downstream of the smooth-to-T9 step change.

During the T9-to-smooth step change, there is a jump in Re_θ (figure 4a). This is due to the near-wall flow acceleration, as reported in the past studies of rough-to-smooth step change (Rouhi et al. 2019). During the step change, there is an overshoot in C_f followed by an undershoot below zero (figure 4b), and then a quick rise towards $C_{f_{SM}}$ within a distance of $\sim \delta_0$ (figure 4c). Such undershoot is also seen in the overlaid rough-to-smooth data of Rouhi et al. (2019) (gray line) and experimental data of Li et al. (2019)

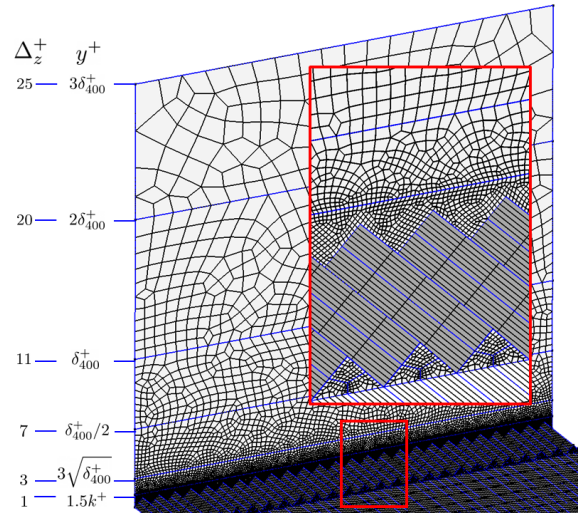


Figure 3: Visualisation of the grid for the case T9_SM on an yz -plane as well as over the riblets and smooth surfaces near the step change. The viscous-scaled spanwise grid size Δ_z^+ is reported at different viscous-scaled wall-normal distances y^+ ; δ_{400}^+ is the viscous-scaled boundary layer thickness at $Re_\tau = 400$ (i.e. $\delta_{400}^+ = 400$).

(symbols).

The undershoot in C_f downstream of the step change, and its subsequent recovery to its equilibrium counterpart ($C_{f_{SM}}$) depends on the high and low shear regions at downstream of the step change, which in turn depend on the geometrical details of the upstream surface, as well as the Reynolds number. Rouhi et al. (2019) conducted DNS of turbulent channel flow over egg-carton roughness to smooth step change at $Re_\tau \simeq 590$ with roughness height $k^+ \simeq 39$. Li et al. (2019) conducted experiments of ZPG TBL over sandpaper to smooth step change at $Re_\tau \simeq 4100$ and $k^+ \simeq 139$. The recovery to $C_{f_{SM}}$ is within $2\delta_0$ in Rouhi et al. (2019) and within $12\delta_0$ in Li et al. (2019). For our present T9.SM case, $C_f/C_{f_{SM}}$ reaches an asymptotic value of ~ 0.97 within $7\delta_0$, but does not recover to 1.0, even after $48\delta_0$ downstream (figure 4c, inset). Note that to calculate $C_f/C_{f_{SM}}$, C_f and $C_{f_{SM}}$ are at matched Re_θ , following Li et al. (2021).

For the SM.T9 case, there is a drop in Re_θ during the step change (figure 5a), due to the momentum deficit and the flow deceleration near the wall. During

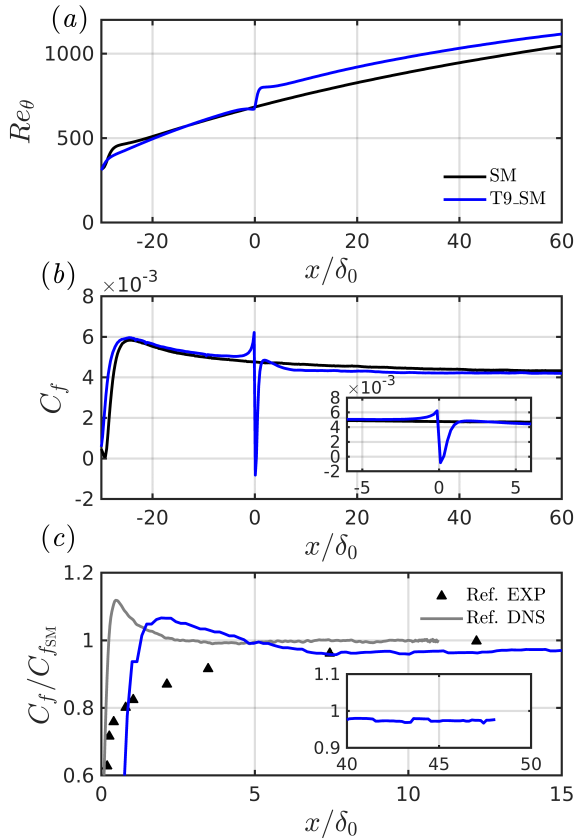


Figure 4: Streamwise variations of (a) Re_θ , and (b,c) C_f for the T9-to-smooth step change. In (a,b) the smooth case (SM) is added as a reference. In (c), C_f for T9.SM is normalized by C_f from the smooth case ($C_{f_{SM}}$) at matched Re_θ ; rough-to-smooth step change data of Rouhi et al. (2019) (Ref. DNS) and Li et al. (2019) (Ref. EXP).

the step change, we observe an undershoot in C_f , followed by an overshoot (figure 5b) consistent with the past studies on smooth-to-rough step change (Rouhi et al. 2019, Cogo et al. 2025). For the SM.T9 case, $C_f/C_{f_{T9}}$ reaches an asymptotic value of 1.04 within $5\delta_0$ (figure 5c), which is shorter than the asymptotic distance for $C_f/C_{f_{SM}}$ for the T9.SM case (figure 4c). Nevertheless, $C_f/C_{f_{T9}}$ does not converge to 1.0, even after $58\delta_0$ (figure 5c, inset). To calculate $C_f/C_{f_{T9}}$, C_f and $C_{f_{T9}}$ are at matched Re_θ .

Downstream of the T9-to-smooth and smooth-to-T9 step changes, C_f converges to within $\pm 4\%$ of its equilibrium counterpart, but does not reach it. We explain this behavior through figure 6(b), by studying the profiles of $dU^+/d\ln(y^+)$ at $6\delta_0$ and $24\delta_0$ downstream of the T9-to-smooth step change (blue curves), compared with the one at $4\delta_0$ upstream of the step change (green curve). Also, for each downstream profile, we overlay the profile from the smooth case (SM) at matched Re_θ (black curves). The internal equilibrium layer thickness (δ_{IEL}) is the y^+ to which the profiles of T9.SM and SM collapse on each other (marked with a magenta bullet). In figure 6(c), we follow a sim-

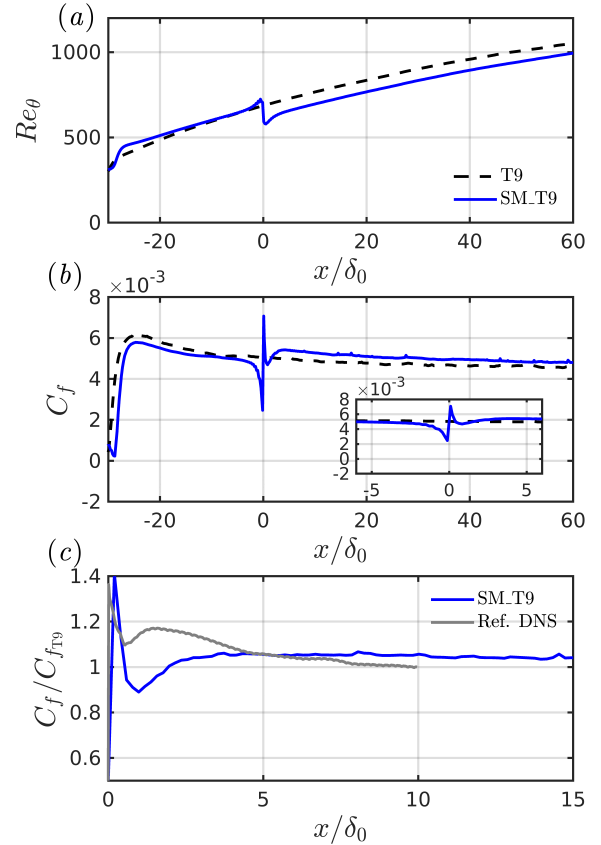


Figure 5: Same quantities as Figure 4 but for SM.T9 step change. In (a,b) the T9 case is added as a reference. In (c), C_f for SM.T9 is normalized by C_f from the T9 case ($C_{f_{T9}}$) at matched Re_θ ; smooth-to-rough step change data of Rouhi et al. (2019) (Ref. DNS).

ilar approach to identify δ_{IEL} based on the agreement in the streamwise turbulent stress profiles $\overline{u'^2}^+$; the resulting δ_{IEL} is almost the same as the one based on $dU^+/d\ln(y^+)$. Considering figure 6(b), at $x = 6\delta_0$, the profiles of T9_SM and SM agree up to $y^+ \simeq 8$ ($\delta_{IEL}^+ \simeq 8$); at $x = 24\delta_0$, the two profiles agree up to a height $y^+ \simeq 70$ ($\delta_{IEL}^+ \simeq 70$). Beyond $y^+ \simeq 70$, the profiles of T9_SM and SM significantly differ from each other, which corresponds to their wake region. Such difference in the wake region persists up to the farthest distance that we simulated. Interestingly, the wake profile of the T9_SM case downstream of the step change (blue curve) is close to its counterpart from upstream of the step change (green curve). This indicates a frozen wake region that preserves its history, and remains uninfluenced by the underneath smooth surface. Since the wake profile of the T9_SM case does not recover to the one from the SM case,

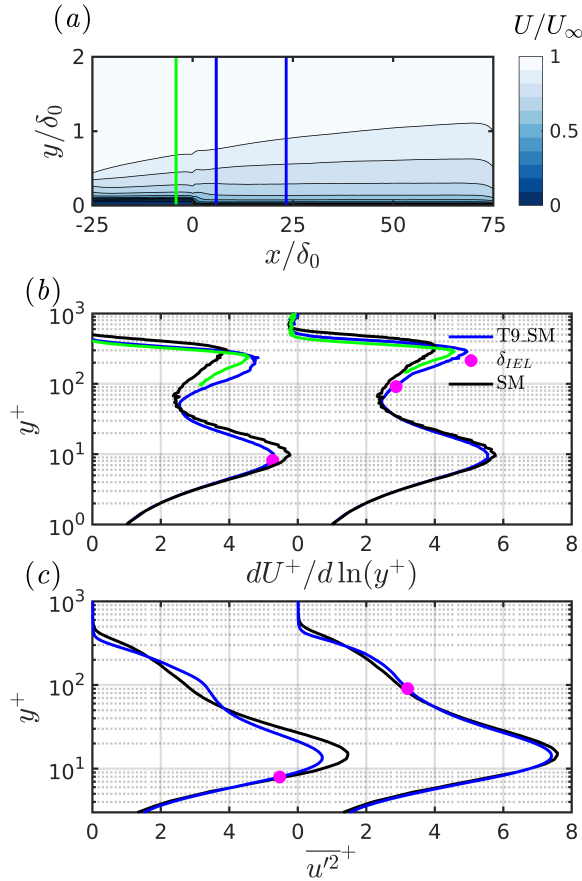


Figure 6: Identification of IEL based on $dU^+/d\ln y^+$ for the T9_SM case. Profiles of (b) $dU^+/d\ln y^+$ and (c) $\overline{u'^2}^+$ at $6\delta_0$ and $24\delta_0$ downstream of the step change, as indicated with vertical dashed lines in (a). At each location, the profiles of T9_SM case are compared with the ones from the smooth case (SM) at matched Re_θ . On each profile, the IEL is located with a magenta bullet. In (b), we overlay the wake profile from $4\delta_0$ upstream of the step change (green line).

$C_f/C_{f_{SM}}$ does not recover to 1.0 (figure 4c). To elaborate more, $C_f \equiv 2\tau_w/(\rho U_\infty^2) \equiv 2/U_\infty^{+2}$, and U_∞^+ is the integral of the $dU^+/d\ln(y^+)$ profile. Therefore, agreement in C_f values requires agreement in the entire $dU^+/d\ln(y^+)$ profiles. For the SM_T9 case, we observe similar frozen wake region with strong history effects, hence $C_f/C_{f_{T9}}$ does not converge to 1.0 (figure 5c).

We study the growth of δ_{IEL} downstream of the T9-to-smooth step change (figure 7a), compared with the one downstream of the smooth-to-T9 step change (figure 7b). Initially, δ_{IEL} stays below $0.1\delta_0$, equivalent to $\delta_{IEL}^+ \lesssim 30$. This initial slow growth corresponds to the recovery in the near-wall turbulence up to the beginning of the logarithmic region. This slow growth continues up to $x \simeq 12\delta_0$ for the T9_SM case, and up to $x \simeq 4\delta_0$ for the SM_T9 case. Thus, the near-wall turbulence has a slower recovery during the T9-to-smooth step change. After the initial slow growth, δ_{IEL} jumps to $\sim 0.4\delta_0$ and does not grow any further. This height is the beginning of the wake region, that remains uninfluenced by the the surface underneath. Thus, δ_{IEL} does not reach the boundary layer thickness.

4 Conclusions

We investigated the recovery of a ZPG TBL downstream of a riblet-to-smooth step change, and vice versa. We focused on drag-increasing triangular riblets with tip angle 90° and viscous-scaled spacing 50 (T9 riblets). The ZPG TBL has $Re_{\theta_0} \simeq 680$ right upstream of the step change, and grows up to $Re_\theta \simeq 1000$

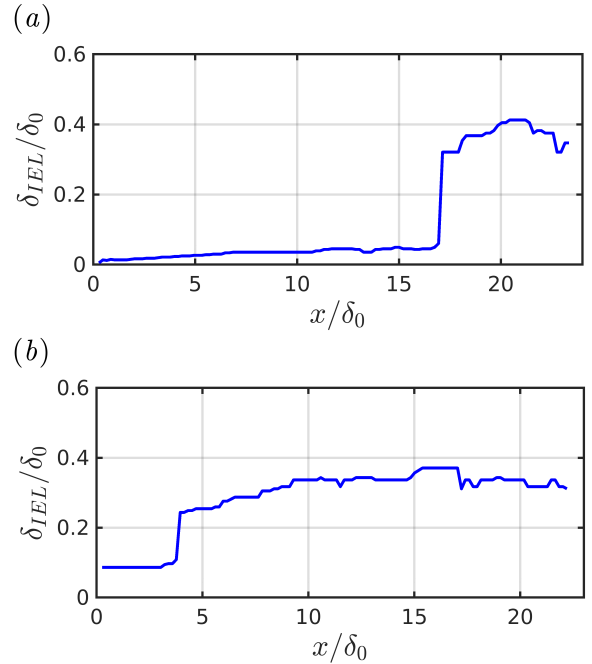


Figure 7: Streamwise growth of IEL thickness δ_{IEL} for (a) riblet-to-smooth step change, and (b) smooth-to-riblet step change.

downstream of the step change. To evaluate the flow recovery to equilibrium, we conducted additional calculations of a ZPG TBL over an entirely smooth wall, as well as one covered entirely by T9 riblets. To make the computations affordable, we proposed a novel grid generation approach for unstructured spectral element solvers, where the elements size grows consistent with the size of turbulent scales. We observed that C_f converged to its equilibrium value with a faster rate during smooth-to-T9 step change (within $4\delta_0$), than during T9-to-smooth step change (within $7\delta_0$). However, for both step changes, C_f did not completely reach equilibrium, even after $45\delta_0$ downstream of the step change. Similarly, the internal equilibrium layer thickness δ_{IEL} did not reach the TBL thickness, and stayed within $0.4\delta_0$. Assessment of the profiles of the mean velocity derivative $dU^+/d\ln(y^+)$ and streamwise turbulent stress $\overline{u'^2}^+$ revealed that the wake region does not recover, even up to $45\delta_0$, leading to the incomplete recovery in C_f and δ_{IEL} .

Acknowledgments

VK acknowledges his AI4S fellowship within the Generación D initiative by Red.es, Ministerio para la Transformación Digital y de la Función Pública, for talent attraction (C005/24-ED CV1), funded by NextGenerationEU through PRTR. AR acknowledges the support from the Air Force Office of Scientific Research (AFOSR) under award number FA8655-24-1-7008, monitored by Dr. Douglas Smith and Dr. Barrett Flake. WW acknowledges the support from AFOSR Grant No. FA9550-25-1-0033, monitored by Dr. Gregg Abate. We thank EPSRC for the computational time made available on ARCHER2 via the UK Turbulence Consortium (EP/R029326/1), and the UKRI access to the HPC call 2024.

References

- Antonia, R. A. & Luxton, R. E. (1971) The response of a turbulent boundary layer to a step change in surface roughness. Part 1. Smooth to rough. *J. Fluid Mech.* 48, 721–761.
- Bannier, A., Garnier, É. and Sagaut, P. (2015). Riblet flow model based on an extended FIK identity. *Flow Turbul. Combust.*, Vol. 95, pp. 351-376.
- Boomsma, A. and Sotiropoulos, F. (2015). Riblet drag reduction in mild adverse pressure gradients: a numerical investigation. *Int. J. Heat Fluid Flow*, Vol. 56, pp. 251-260.
- Chen, C. & He, L. 2023 Two-scale solution for tripped turbulent boundary layer. *J. Fluid Mech.* 955, A5.
- Choi, K.S. (1989). Near-wall structure of a turbulent boundary layer with riblets. *J. Fluid Mech.*, Vol. 208, pp. 417-458.
- Cogo, M., Modesti, D., Bernardini, M. and Picano, F. (2025). Surface roughness effects on subsonic and supersonic turbulent boundary layers. *J. Fluid Mech.*, Vol. 1009, p. A56.
- Endrikat, S., Modesti, D., Garcia-Mayoral, R., Hutchins, N. and Chung, D. (2021). Influence of riblet shapes on the occurrence of Kelvin–Helmholtz rollers, *J. Fluid Mech.*, Vol. 913, pp. A37.
- Garratt, J. R. (1990). The internal boundary layer - A review. *Boundary-Layer Meteorol.*, 50(1–4), 171–203.
- Gasparino, L., Spiga, F., & Lehmkuhl, O. (2024). SOD2D: A GPU-enabled Spectral Finite Elements Method for compressible scale-resolving simulations. *Comput. Phys. Commun.*, 297, 109067.
- Guermond, J.-L., Pasquetti, R., & Popov, B. (2011). Entropy viscosity method for nonlinear conservation laws. *J. Comput. Phys.* 230(11), 4248–4267.
- Ismail, U., Zaki, T. A., & Durbin, P. A. (2018). Simulations of rib-roughened rough-to-smooth turbulent channel flows. *J. Fluid Mech.*, 843, 419–449.
- Karniadakis, G. E., Israeli, M., & Orszag, S. A. (1991). High-order splitting methods for the incompressible Navier-Stokes equations. *J. Comput. Phys.* 97(2), 414–443.
- Li, M., de Silva, C. M., Rouhi, A., Baidya, R., Chung, D., Marusic, I., & Hutchins, N. (2019). Recovery of wall-shear stress to equilibrium flow conditions after a rough-to-smooth step change in turbulent boundary layers. *J. Fluid Mech.*, 872, 472–491.
- Li, M., De Silva, C.M., Chung, D., Pullin, D.I., Marusic, I. and Hutchins, N. (2021). Experimental study of a turbulent boundary layer with a rough-to-smooth change in surface conditions at high Reynolds numbers. *J. Fluid Mech.*, Vol. 923, p. A18.
- Modesti, D., Endrikat, S., Hutchins, N., & Chung, D. (2021). Dispersive stresses in turbulent flow over riblets. *J. Fluid Mech.*, 917, A55.
- Munters, W., Meneveau, C. and Meyers, J. (2016). Turbulent inflow precursor method with time-varying direction for large-eddy simulations and applications to wind farms. *Boundary Layer Meteorol.*, Vol. 159, pp. 305-328.
- Rouhi, A., Chung, D., & Hutchins, N. (2019). Direct numerical simulation of open-channel flow over smooth-to-rough and rough-to-smooth step changes. *J. Fluid Mech.*, 866, 450–486.
- Rouhi, A., Endrikat, S., Modesti, D., Sandberg, R. D., Oda, T., Tanimoto, K., Hutchins, N. & Chung, D. (2022) Riblet-generated flow mechanisms that lead to local breaking of reynolds analogy. *J. Fluid Mech.* 951, A45.
- Savelyev, S. A. & Taylor, P. A. (2005) Internal boundary layers: I. Height formulae for neutral and diabatic flows. *Boundary-Layer Meteorol.* 115, 1–25.
- Schlatter, P., Örlü, R., Li, Q., Brethouwer, G., Fransson, J. H. M., Johansson, A. V., Alfredsson, P. H., & Henningson, D. S. (2009). Turbulent boundary layers up to $Re_\theta = 2500$ studied through simulation and experiment. *Phys. Fluids*, 21(5).
- Vreman, A.W. (2004). An eddy-viscosity subgrid-scale model for turbulent shear flow: Algebraic theory and applications. *Phys Fluids*, Vol. 16, pp. 3670-3681.